*Carbon Energy*

WILEY

CARBON ENERGY

RESEARCH ARTICLE OPEN ACCESS

# Simultaneous Photoactivation of Copper and Ti-Doped $CeO_{2-x}$ Enables Optimal Acceleration of the RWGS Reaction

Miha Okorn[1,2] | Kristijan Lorber[1] | Matjaž Mazaj[1] | Nataša Novak Tušar[1,2] | Petar Djinović[1,2]

[1]Department of Inorganic Chemistry and Technology, National Institute of Chemistry, Ljubljana, Slovenia | [2]University of Nova Gorica, Nova Gorica, Slovenia

**Correspondence:** Petar Djinović (petar.djinovic@ki.si)

**Received:** 20 May 2025 | **Revised:** 2 July 2025 | **Accepted:** 9 August 2025

**Funding:** Slovenian Research and Innovation Agency (ARIS) financed this research through projects N2-0265 and P1-0418.

**Keywords:** $CO_2$ hydrogenation Cu/$CeO_2$ catalyst | in situ spectroscopy | light-assisted catalysis | reaction mechanism

## ABSTRACT

Light-assisted catalysis is a promising approach for accelerating the thermally driven catalytic reverse water gas shift (RWGS) reaction, which converts $CO_2$ and $H_2$ into valuable CO. In this work, pure $CeO_2$ nanorods and titanium-modified $CeO_2$ nanorods were functionalized with 1–30 wt.% of copper. The catalyst containing 3 wt.% of copper (3Cu–$CeTiO_2$) was the most active for the light-assisted RWGS reaction. Illuminating the 3Cu–$CeTiO_2$ catalyst with 770 mW $cm^{-2}$ of visible light resulted in a CO rate, which was up to 57 times higher than that under purely thermal conditions at identical catalyst temperature. Catalyst illumination with wavelengths shorter than 450 nm triggers simultaneous photoexcitation of the Ti-doped $CeO_{2-x}$ support and Cu nanoparticles. This accelerates the RWGS reaction approximately twofold more, compared to excitation of the copper phase alone. Copper is responsible for $H_2$ dissociation, the Cu–$O_v$–Ce interface active sites enable the catalytic reaction, and titanium doping diminishes emissive recombination, making photoexcitation more efficient. Furthermore, the $E_a$ for CO formation decreased drastically from 92 to 26 kJ $mol^{-1}$ during the light-assisted reaction, revealing a change of the reaction mechanism and lowered energetics of the rate-determining step. Our kinetic analysis and *operando* DRIFTS analysis suggest that hydrogen species chemisorb more strongly under illumination, and the most abundant surface species (carbonates and formates) hydrogenate and dissociate faster, resulting in accelerated CO formation.

## 1 | Introduction

Fossil fuels serve as the primary energy source and significantly contribute to the rapidly increasing $CO_2$ emissions into the atmosphere. This intensifies the pressing global issues of climate change and global warming [1]. As we face the energy crisis, fueled by the increasing depletion of fossil fuel reserves and large $CO_2$ generation, action is needed to utilize alternative and sustainable energy solutions. One of the most promising candidates for renewable energy is the endless potential of sunlight, which has no directly associated $CO_2$ footprint, but is highly fluctuating and is currently not yet cost-effective [2].

Strategies for $CO_2$ conversion into added-value chemicals have garnered attention as essential pathways toward carbon neutrality. $CO_2$ hydrogenation to hydrocarbons (Fischer–Tropsch synfuels or methane) and different alcohols [3–7], or to CO via the reverse water gas shift (RWGS) reaction is at the center of research as strategies for large-scale carbon capture and utilization (CCU). However, RWGS reaction requires high temperatures (> 700°C) and $H_2$ surplus to ensure sufficiently high $CO_2$

conversion (Figure S1 and Equation 1) [7, 8]. In turn, this presents challenges like catalyst sintering and deactivation, as well as energy inefficiency.

$$CO_2 + H_2 \leftrightarrow CO + H_2O \quad \Delta H^{\circ}_{R298\,K} = 41\ \text{kJ mol}^{-1} \qquad (1)$$

To address these challenges, we need to unlock sustainable RWGS routes that capitalize on higher catalytic activity and renewable energy. Combining sunlight as an abundant and sustainable energy source and a suitable photo catalyst offers a potential solution to develop an efficient RWGS process that operates with high rates closer to ambient conditions, and improves maximum achievable CO yield while maintaining high catalyst stability.

Catalysts in photothermal reactions are usually composite materials comprising semiconductors and/or (plasmonic) materials, which contain suitable catalytic sites and light-harvesting properties [9]. Typical optical response of plasmonic materials to light with a suitable wavelength is localized surface plasmon resonance (LSPR), where light interacts with free conduction band electrons on the surface of plasmonic nanoparticles (NPs). Plasmon-induced effects, which influence photocatalytic activity, can be divided into three categories: (1) enhancement of the near (local) electromagnetic field, (2) hot carrier generation induced by plasmon decay in the metal NP, and (3) strong local heating of the NP due to thermalization of high-energy (hot) carriers. Hot carriers (electrons and holes) can transport from metal NPs to the adsorbed molecules or the semiconductor by either direct or indirect transfer and thereby participate in the catalytic process [2, 10]. This enables nonthermal reaction channels to occur, making conversion and selectivity no longer limited by the thermodynamic equilibrium [9, 11, 12].

Ag and Au exhibit strong LSPR, yet due to their limited availability and high cost, there is a lot of focus on finding alternative metals with plasmonic properties, such as Al and Cu. Copper-based catalysts are widely studied materials for the thermally driven catalytic $CO_2$ hydrogenation to CO or methanol [5, 13, 14] due to their low cost, as well as good activity and selectivity. Several studies have shown that $CeO_2$ decorated with Cu shows high activity in the RWGS reaction and simultaneously shows negligible selectivity toward the methanation side reaction [5, 15]. The LSPR of metallic copper can be induced by photons with wavelengths around 600 nm, making it a suitable visible light-driven photocatalyst [16]. However, the main challenge of Cu in the photocatalytic reactions is oxidation when exposed to oxygen or water vapor. Oxidation of Cu to $Cu_2O$ or CuO quenches its plasmonic properties [17].

Many oxide-supported metal catalysts have been explored for $CO_2$ conversion to CO, $CH_4$, and methanol, with cerium oxide ($CeO_2$) playing a central role [18]. Additionally, Ce-based catalysts have shown great potential in various light-assisted reactions, including but not limited to $CO_2$ reduction, hydrogenation, and low-temperature $NO_x$ removal [19–21]. Under reducing conditions and elevated temperature, its unique electron arrangement facilitates the formation of surface and bulk oxygen vacancies [22], as well as reversible and fast redox pair switching ($Ce^{3+} \leftrightarrow Ce^{4+}$). Thermal stability and the ability to effectively disperse metal NPs due to the strong metal–support interactions further enhance the catalytic activity at the metal–support interface [23]. Nanoshaping of $CeO_2$ can further improve its redox catalytic activity through exposure of {111}, {110}, and {100} terminating facets [24, 25]. In ceria nanorods, the abundance of {110} facets, which exhibit the lowest energy for oxygen vacancy formation, is maximized [25, 26]. Furthermore, Lorber et al. demonstrated that oxygen deficiency of ceria nanorods considerably narrowed its bandgap, making substoichiometric ceria capable of acting as a visible photon-responsive semiconductor [21]. Liyanage et al. reported that Y-doped and pure $CeO_2$ nanorods showed the optical bandgap of 2.63 and 2.68 eV, which means that they can absorb and utilize visible light [27]. Combining $CeO_2$ nanorods with $TiO_2$ (a well-known photocatalyst) or doping with $Ti^{4+}$ was previously shown to positively affect the photocatalytic RWGS performance [28, 29].

In this work, different amounts of copper were deposited on bare and titanium-modified $CeO_2$ nanorods, which were analyzed for their activity during thermal and visible light-assisted RWGS reaction. Kinetic analysis was complemented with structural and spectroscopic characterization to shed light on the reaction mechanism and the underlying phenomena that enable significant acceleration of the RWGS rate under illumination.

## 2 | Results and Discussion

### 2.1 | Catalytic Activity

Initial catalytic tests were performed on $CeO_2$ and titanium-doped (0.5 mol.%) $CeO_2$ supports containing different amounts of copper (1, 3, 8, and 30 wt.%, denoted as *x*Cu–CeTi, where *x* represents the copper content). The catalyst temperature was fixed at 300°C and equimolar $H_2/CO_2$ feed (Figure 1A) or excess $H_2$ ($H_2/CO_2 = 2.4/1$, Figure S2A) were used. Generally, titanium-doped catalysts enabled higher CO formation rates compared to analogous $CeO_2$-based catalysts during dark- and light-assisted reactions, indicating a beneficial effect of titanium addition to $CeO_2$. The only exception was the 30Cu–CeTi sample, but its performance was much inferior compared to all other samples. When comparing the effect of copper content (1, 3, 8, and 30 wt.%) on CO rates, the following trend in catalytic activity was observed: 3Cu–CeTi > 8Cu–CeTi ≈ 1Cu–CeTi > 30Cu–CeTi. The 1Cu–CeTi and 8Cu–CeTi catalysts both exhibited similar CO rates under dark-assisted (0.4 and 0.44 mmol $g_{cat}^{-1}$ $min^{-1}$) and light-assisted conditions (1.47 and 1.74 mmol $g_{cat}^{-1}$ $min^{-1}$). In all experiments, CO was produced with 100% selectivity. The 3Cu–CeTi catalyst demonstrated the highest catalytic activity both under dark- and light-assisted conditions (0.56 and 2.6 mmol $g_{cat}^{-1}$ $min^{-1}$, respectively). Consequently, 3 wt.% is the optimal copper loading in our tested catalysts. Based on these preliminary examinations, further tests were performed with the 3Cu–CeTi catalyst. Zhou et al. also observed a volcano-type activity dependence when varying the Cu loading in the $Cu/CeO_2$ catalysts for the RWGS reaction. However, in their study, the samples containing 8 wt.% of Cu proved to be the most active [30].

The CO rate produced by the 3Cu–CeTi catalyst was also analyzed with a $H_2/CO_2 = 2.4/1$ feed ratio (Figure 1B). Excess $H_2$ led to a marginal increase in the dark, whereas a strong negative

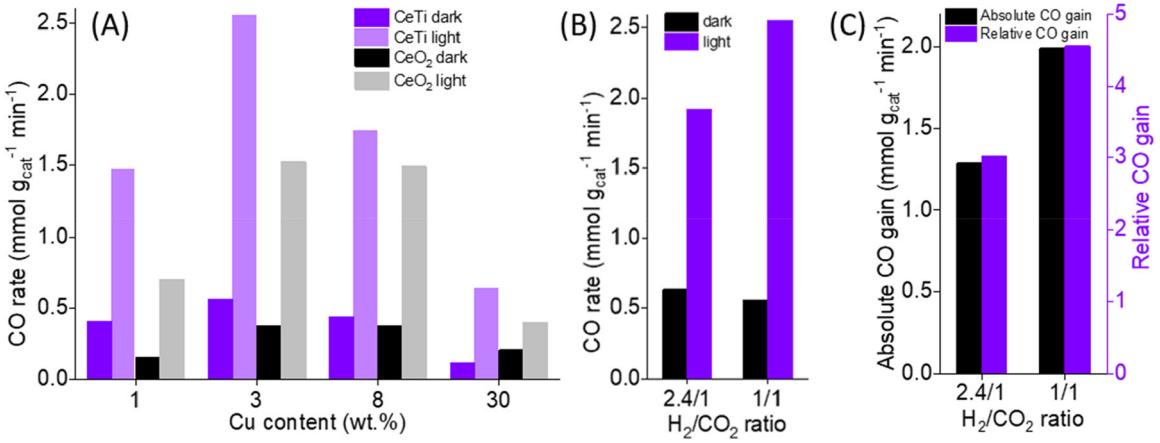


**FIGURE 1** | (A) CO rate comparison under thermocatalytic and light-assisted conditions for different copper loadings deposited on $CeO_2$ and CeTi supports using the inlet gas $H_2/CO_2$ ratio of 1/1. (B) CO rate for 3Cu–CeTi catalyst using different $H_2/CO_2$ feed ratios and (C) absolute and relative CO rate gains derived from data in (B). In all experiments, the total flow was equal to 30 mL $min^{-1}$. During light-assisted reaction, the catalysts were illuminated by 770 mW $cm^{-2}$ of white light, and the external heating was adjusted to maintain the catalyst temperature constant at 300°C.

effect on the CO rate was observed under light-assisted conditions. Under thermally driven conditions in excess hydrogen, trace amounts of methane were formed, lowering the CO selectivity to 97%. On the contrary, under light-assisted RWGS conditions, selectivity to CO was restored to 100%, which is in line with previous research on light-assisted RWGS over $Cu/Al_2O_3$ [31]. The benefits of light-assisted RWGS are shown in Figure 1C as absolute CO gain (light-assisted CO rate minus the dark CO rate) and relative CO rate gains (light-assisted CO rate/dark CO rate). CO formation was maximized at equimolar $H_2/CO_2$ feed, and illumination enables a 4.5-fold acceleration of the CO rate compared to dark conditions, which equals 2 mmol CO $g_{cat}^{-1}$ $min^{-1}$.

The 3Cu–CeTi catalyst was further analyzed with temperature-dependent experiments (Figure 2A). The CO rate increased with temperature under dark and illuminated conditions. The rates were substantially higher in the light-assisted reaction throughout the entire temperature range, and no deactivation was observed. Below 213°C, there is no catalytic activity in the dark, whereas 0.24 mmol CO $g_{cat}^{-1}$ $min^{-1}$ was produced under sample illumination without additional electric heating, where the catalyst operated at 116°C. At all temperatures, CO was produced with 100% selectivity.

Figure 2B shows the temperature-dependent absolute and relative CO gains with the 3Cu–CeTi catalyst. Relative CO gain increases from 3 to 57 as the temperature decreases from 320°C to 210°C, indicating that the light-driven contribution becomes progressively dominant at lower catalyst temperatures. This is because of the exponential (Arrhenius-type) temperature dependence of the thermally driven catalytic reaction, whereas the light-driven contribution depends on the number of photons, which was constant. Higher temperatures also favor recombination of charges and cause plasmons to decay more rapidly, therefore minimizing the effects of pure photochemical contribution. Upadhye et al. observed a similarly decreasing CO gain with increasing temperature over the illuminated $Au/TiO_2$ catalyst [32]. Absolute CO rate gain using the 3Cu–CeTi catalyst, however, increased with temperature from 0.90 to 1.99 mmol $g_{cat}^{-1}$ $min^{-1}$, which can be attributed to light-induced excitation of the CeTi support and the increase of the ground state energy of the CeTi valence band due to higher temperatures. Additionally, the surface population with spectator species becomes less dense with increasing temperature [23], resulting in more free sites that accommodate reaction intermediates [33]. The stability of the 3Cu–CeTi catalyst was evaluated at 270°C under both dark- and light-assisted conditions (Figure 2C). In both cases, the catalytic activity decreased over the initial 30 h on stream, after which it reached a steady state. The initial CO rates decreased by 34% in the dark-assisted and 31% in light-assisted conditions, respectively, revealing similar catalyst deactivation extent. While light irradiation does not influence the long-term stability of the catalyst, it results in a notably (10-fold) enhanced catalytic activity.

Arrhenius plots for the 3Cu–CeTi catalyst (Figure 2D) showed that the apparent activation energy value ($E_a$) decreased from 92 to 26 kJ $mol^{-1}$ upon illumination. This dramatic $E_a$ drop reveals a change in the reaction mechanism and decreased energy barrier of the rate-determining step of the reaction. The $E_a$ value for the 30Cu–CeTi catalyst under dark conditions (88 kJ $mol^{-1}$) was very similar to that of the 3Cu–CeTi catalyst, but dropped only to 57 kJ $mol^{-1}$ upon illumination. This reveals that the RWGS reaction mechanism under illumination is different among the two samples, Figure S2B.

To further analyze the light-induced changes of the RWGS reaction channel, variable irradiance experiments were performed, Figure 2E. By increasing the illumination of the catalyst, resistive heating was decreased, thus maintaining a constant catalyst temperature of 270°C. The CO rate was modestly influenced in the low-irradiance range (< 400 mW $cm^{-2}$) and only after exceeding 400 mW $cm^{-2}$ did the CO rate increase linearly with the number of photons. Full intensity illumination with 770 mW $cm^{-2}$ accelerated the CO formation almost 10-fold compared to reaction in the dark at identical catalyst temperature: from 0.26 to 2 mmol $g_{cat}^{-1}$ $min^{-1}$, thus confirming the dominant role of light on CO formation. Marimuthu et al. [34] observed a threshold irradiance of about 550 mW $cm^{-2}$ during the light-assisted propylene epoxidation

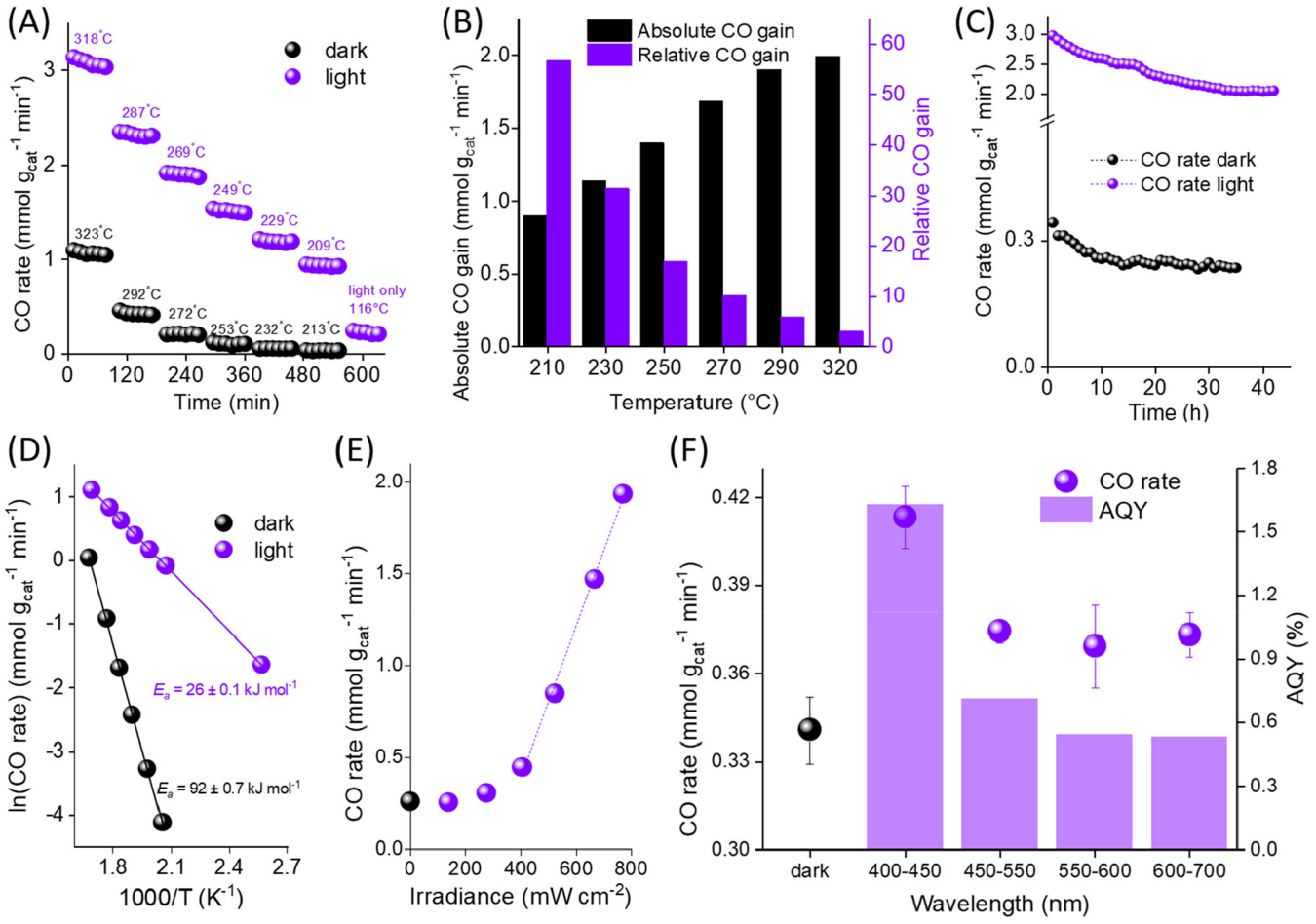


**FIGURE 2** | (A) Temperature dependence of the CO rate under dark- and light-assisted conditions. (B) Temperature-dependent relative and absolute CO rate gain. (C) Long-term thermocatalytic and light-assisted RWGS activity at 270°C. (D) Apparent activation energy values ($E_a$) under dark- and light-assisted conditions. (E) Dependence of the CO rate on irradiance. (F) CO rate and apparent quantum yield (AQY) at different excitation ranges, a constant irradiance of 230 mW cm$^{-2}$, and a temperature of 270°C. Black dot shows the CO rate in the dark. All data relate to the 3Cu–CeTi catalyst. In all these experiments, the flow rate of $H_2/CO_2$ gas feed was kept constant at 30 mL min$^{-1}$.

reaction using molecular oxygen and Cu/$SiO_2$ catalysts. They reasoned that a sufficiently high irradiance is required to maintain the metallic form of copper and prevent its oxidation to $Cu_2O$, thus enabling its LSPR property to drive the light-assisted catalytic reaction. In our case, the irradiance threshold is lower, likely due to the use of a softer oxidant ($CO_2$ has a lower oxidizing power compared to $O_2$) and because copper tends to remain in a metallic state when deposited on ceria compared to silica, due to electronic metal–support interactions and altered charge redistribution [35]. In line with this reasoning, Xie et al. observed that illumination with visible light (420–800 nm) of the Cu–ZnO–$Al_2O_3$ material in the $H_2/CO_2$ flow increases the $Cu^0/Cu^{1+}$ fraction in the catalyst [36].

Next, different wavelength ranges were used to individually (or collectively) excite $CeTiO_{2-x}$ support, Cu inter- and intraband transitions, and LSPR (Figure 2F). Catalyst temperature was maintained constant at 270°C throughout the experiment. When illuminated with wavelengths between 450 and 550 nm (Cu interband transitions), 550–600 nm (Cu LSPR), and 600–700 nm (Cu intraband transitions), the catalyst produced CO with a rate of 0.37 mmol $g_{cat}^{-1}$ min$^{-1}$, which is 10% higher compared to the reaction in the dark. However, a 20% gain in CO rate compared to the experiment in the dark (0.41 mmol $g_{cat}^{-1}$ min$^{-1}$) was observed upon illumination with photons in the 400–450 nm range. This difference could be attributed to the simultaneous excitation of the $CeTiO_{2-x}$ support (bandgap = 3.06 eV, Table S4), as well as the Cu interband transitions. The calculated apparent quantum yield (AQY) values (Figure 2F) correlate with the light-induced CO rate acceleration and reach 1.6% for excitation with photons in the 400–450 nm range. Comparison of CO rates and AQY values between the 3Cu–CeTi catalyst and different catalyst formulations used in light-assisted RWGS (Table S1) shows very competitive performance and efficiency of the catalyst used in this work.

Kinetic analysis was performed by exploring the dependence of the dark and illuminated CO rates on $CO_2$ and $H_2$ partial pressures (i.e., concentrations), and then calculating the corresponding reaction orders (Figure 3). This way, we investigated the light-induced differences in the RWGS reaction mechanism. The Langmuir–Hinshelwood type reaction mechanism is rationally proposed (both reactants chemisorbed on the catalyst surface), since our control experiments ruled out the existence of redox (Mars–van Krevelen) reaction mechanism under dark- or light-assisted conditions, Figure S3. As a result, the RWGS

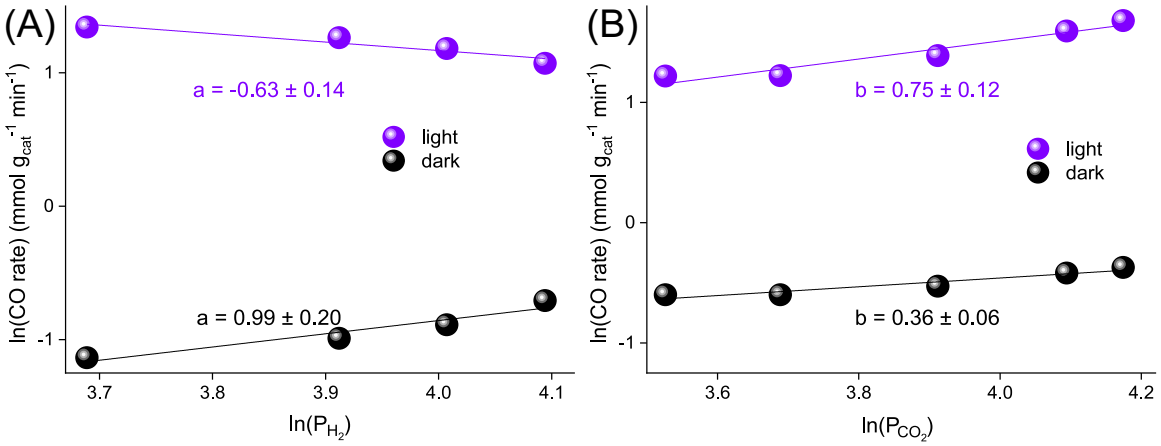


**FIGURE 3** | Dependence of the CO rate on (A) $CO_2$ concentration and (B) $H_2$ concentration over the 3Cu–CeTi catalyst under dark- and light-assisted conditions. These experiments were done at 270°C and 30 mL $min^{-1}$of $H_2/CO_2$ gas feed. During the light-assisted reaction, the sample was irradiated by 770 mW $cm^{-2}$ of visible light.

reaction can be expressed as $r = k{\cdot}(p_{H_2})^a{\cdot}(p_{CO_2})^b$ with $k$ representing the pre-exponential factor, whereas $a$ and $b$ are reaction orders for $H_2$ and $CO_2$, respectively.

Under thermocatalytic conditions (black circles), the reaction order pertaining to $H_2$ is 0.99 and exceeds that of $CO_2$, which is 0.36 (Figure 3A,B). Higher $H_2$ reaction order compared to $CO_2$ under dark conditions suggests that the overall RWGS rate is hindered by a slow reaction step involving either hydrogen dissociation ($H_2$ dissociation energy is estimated as 0.55 eV on Cu(111) and 1.0 eV on Ce(111) surface) [37, 38], or high H diffusion barrier (1.8 eV over the $CeO_2$(111) surface) [37] to reach the active sites, which are located at the copper–ceria interface [5, 31].

Under light-assisted conditions, the reaction order of $H_2$ decreases to a negative value of −0.63. The negative $H_2$ order reveals overcrowding of active sites, which diminishes the abundance of free sites that remain available for $CO_2$ dissociation. As a result, the reaction rate becomes progressively more dependent on $CO_2$ partial pressure and thus $CO_2$ surface coverage, which manifests in the rise of $CO_2$ reaction order to 0.75 [39].

To summarize, our catalytic experiments, kinetic analysis, as well as wavelength and irradiance-dependent experiments show a substantial light-driven change of the RWGS reaction channel. The CO rate is strongly accelerated under visible light illumination, and simultaneous excitation of copper and the $CeTiO_2$ is required to optimally utilize the photon energy.

## 2.2 | Structural Characterization

Inspired by the abovementioned catalytic results, we proceeded with morphological and elemental composition analyses. SEM-EDX elemental analysis confirmed that the actual copper content is very close to the nominal values of 1, 3, 8, and 30 wt.%, Table S2. Titanium content in the CeTi supports varies between 0.34 and 0.56 wt.%, Table S2. All catalysts form agglomerates of interwoven $CeO_2$ nanorods, which vary in length between 20 and 130 nm, Figure 4A3–A5. A segregated CuO phase was observed only in the 30Cu–CeTi sample, Figure 4B2.

The structural properties were analyzed by $N_2$ physisorption and are summarized in Figure S4 and Table S3. All samples exhibit Type II isotherms, characteristic of mesoporous materials with interparticle porosity. The titanium modification of the $CeO_2$ nanorods does not affect the specific surface area (92 $cm^3 g^{-1}$). Depositing 1 and 3 wt.% of copper slightly decreases the Brunauer–Emmett–Teller (BET) specific surface area, while higher copper loadings lead to a more pronounced surface area drop.

The XRD analysis of pure $CeO_2$, CeTi, as well as the 1Cu–CeTi, 3Cu–CeTi, and 8Cu–CeTi samples showed only the diffraction lines of $CeO_2$ (PDF #81-792), Figure S5A [40]. No diffractions corresponding to CuO were observed, due to the low copper loading and its high dispersion. In the 30Cu–CeTi sample, two additional peaks appeared at 35.5° and 38.7°, attributable to CuO (PDF # 01-080-1916), Figure S5B. This is in line with SEM visualization (Figure 4) and pulse $N_2O$ chemisorption data (Table S4), which identified a gradual increase of the average copper particle size from 1.5 to 18 nm as the copper content increased from 3 to 30 wt.%.

With $H_2$-TPR analysis, we probed the redox properties of the synthesized catalysts and obtained indirect information on copper morphology. With increasing copper content, the reduction shifts to higher temperatures, individual contributions change and become progressively more overlapping, indicative of copper particle size growth, Figure S6A. The quantification of $H_2$ consumed during analysis enabled complete reduction of copper and 20–21% reduction of $Ce^{4+}$ to $Ce^{3+}$, Table S4. The exception was the 30Cu–CeTi sample, where only 11% $Ce^{4+}$ to $Ce^{3+}$ reduction was achieved. This is likely due to higher segregation of copper and lower copper–ceria interface, which results in less efficient hydrogen spillover to ceria, which dictates the extent of ceria reduction in the Cu–$CeO_2$ mixed oxide composites [41]. Bare $CeO_2$ and CeTi supports showed negligible reactivity with $H_2$ below 320°C, with reduction dynamics being more prominent at higher temperatures, Figure S6B. Incorporation of Ti into the ceria structure resulted in a shift of the reduction profile of the doped sample to lower temperatures by about 20°C, and the reduction maximum was achieved at 478°C compared to 529°C

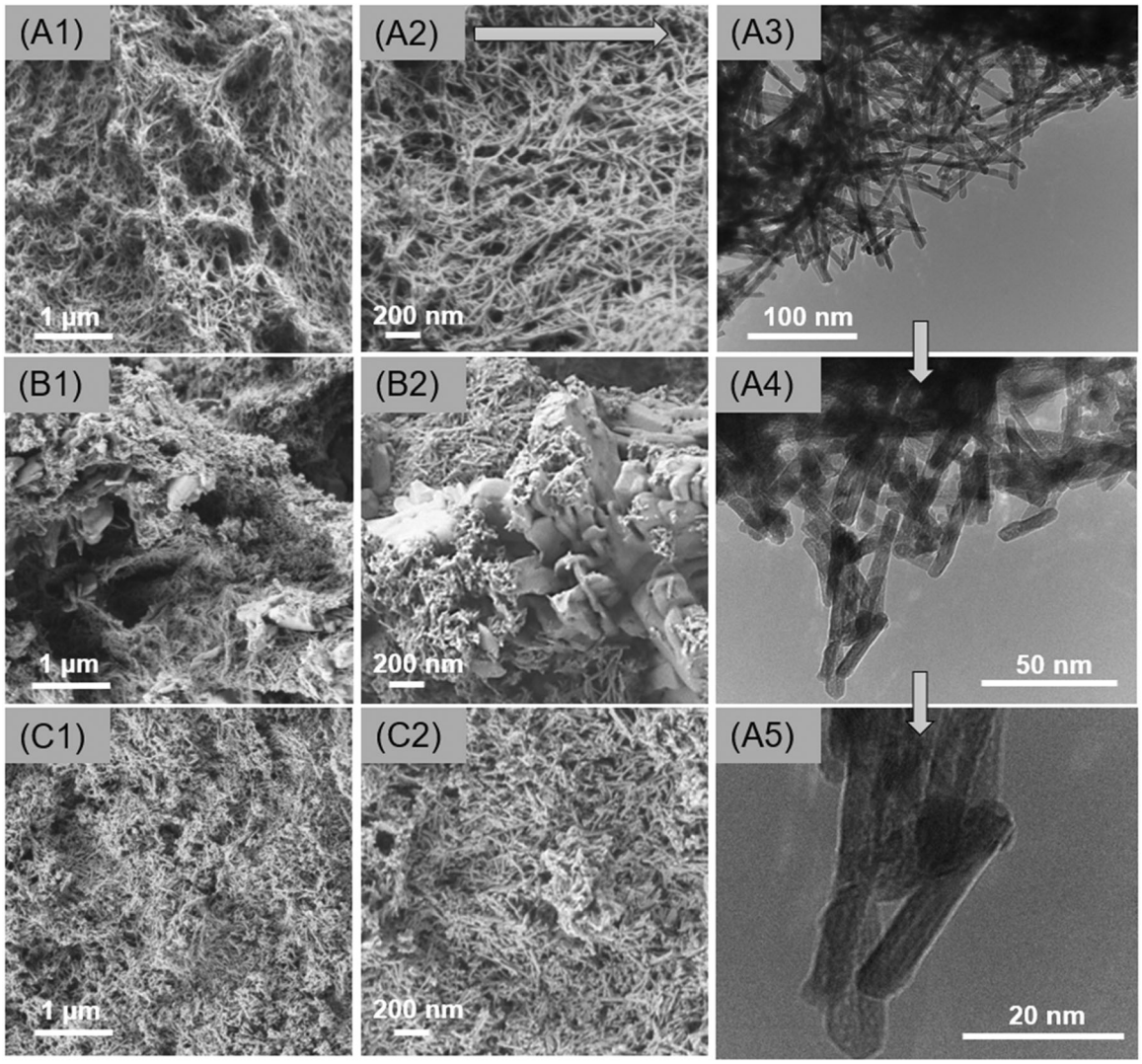


**FIGURE 4** | (A1, A2) SEM images of 3Cu–CeTi catalyst, (B1, B2) 30Cu–CeTi catalyst, and (C1, C2) 3Cu–$CeO_2$ catalyst. (A3–A5) TEM images of the 3Cu–CeTi catalyst.

for pure ceria. However, the extent of $Ce^{4+} \rightarrow Ce^{3+}$ transformation at 550°C remained unchanged for both samples: 19% and 20% for $CeO_2$ and $CeTiO_2$, respectively.

The negative reaction orders of $H_2$ during kinetic analysis (Figure 3A) suggest increased surface hydrogen coverage on the illuminated catalyst. This was verified using $H_2$ pulse chemisorption followed by $H_2$-TPD (temperature programmed desorption) under both dark and illuminated conditions (Figure S7). On the illuminated catalyst, the amount of desorbed $H_2$ equaled $2.2 \times 10^{-4}$ mol $g_{cat}^{-1}$, whereas on the catalyst in the dark, the amount was about 5 times lower, namely $4 \times 10^{-5}$ mol $H_2$ $g_{cat}^{-1}$. If we consider that hydrogen resides on the catalyst in dissociated atomic form (H*) and the abundance of surface atomic copper sites from the CO chemisorption experiment (Table S4) equals to $7.9 \times 10^{-5}$ mol Cu $g_{cat}^{-1}$, the H* density under illumination surpasses the monolayer CO coverage, confirming the light-assisted H* spillover to the ceria support, as suggested also by Yang et al. [42]

Raman analysis was performed to analyze the role of $Ti^{4+}$ and copper on the generation of defects in the $CeO_2$ lattice. Spectra of all samples are dominated by the lattice $F_{2g}$ band of fluorite ceria, which is for the bare $CeO_2$ centered at 460 $cm^{-1}$, Figure 5A,C. The main $F_{2g}$ band of ceria is accompanied by bands located at 595 $cm^{-1}$ (dislocated oxygen, Frenkel-type defects) and 545 $cm^{-1}$ (assigned to oxygen vacancies in the bulk), Figure 5B [33, 43, 44]. The $F_{2g}$ band position abruptly redshifts to 445 $cm^{-1}$ when copper loading reaches 3 wt.%, indicating a change of the Ce–O bond distance, Figure 5C. Interestingly, the Frenkel-type defects (oxygen dislocations in ceria, 595 $cm^{-1}$) are totally attenuated as copper content reaches 3 wt.% and the new band appears at 545 $cm^{-1}$, which is assigned to the presence of oxygen vacancies in ceria, Figure 5D [33]. We assume that the initially present oxygen dislocations in ceria are eliminated at the expense of oxygen vacancy formation, which is due to $Cu^{2+}$ embedding into the ceria structure. To maintain the electroneutrality of the ceria material, a part of $Ce^{4+}$ is reduced to $Ce^{3+}$, causing the formation of Cu–$O_v$–$Ce^{3+}$ interfacial sites. As a result, the catalytically and photocatalytically active 3Cu–CeTi catalyst apparently benefits from oxygen vacancy presence coexisting with highly dispersed copper species (75% dispersion of copper was calculated for the 3Cu–CeTi sample, Table S4), giving rise to the abundance of the Cu–$O_v$–$Ce^{3+}$ active interfacial sites.

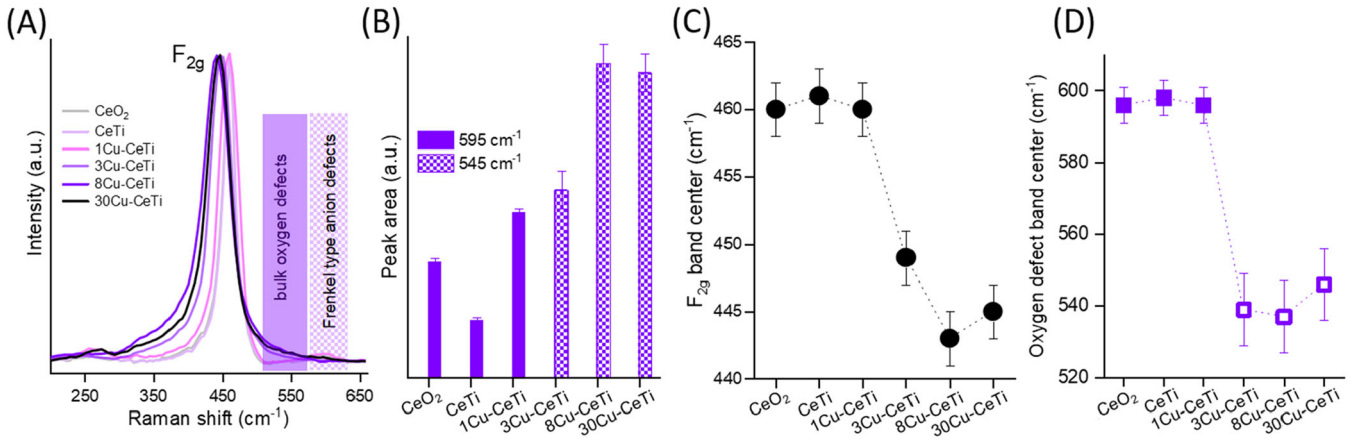


**FIGURE 5** | (A) Raman spectra of $CeO_2$, CeTi support, and Cu–CeTi catalysts containing different amounts of copper. (B) Integrated peak areas for bulk oxygen defects (545 $cm^{-1}$) and oxygen dislocations (595 $cm^{-1}$), (C) $F_{2g}$ band center as a function of copper content, and (D) oxygen defect band center as a function of copper content.

## 2.3 | UV–Vis Spectroscopy and Photoluminescence

The UV–Vis spectra were recorded at room temperature in air (representative of the as-synthesized, fully oxidized samples) and at 270°C in $H_2/CO_2$ flow (active catalyst under working RWGS conditions), Figure 6A–E. The bandgaps of the catalysts were calculated according to the procedure suggested by Makuła et al. [45]. At room temperature, all samples exhibited strong absorption only in the UV region, and the calculated indirect bandgap values were between 2.92 and 3.21 eV (Table S4). Under RWGS reaction conditions, the bandgaps reduced to 2.82–3.17 eV, Figure 6F. This is a consequence of the partial reduction of $Ce^{4+}$ to $Ce^{3+}$ and filling of the otherwise empty 4f orbital of cerium, which lies within the bandgap of ceria [21, 46]. The increase of copper content marginally increased the bandgap, with the 1Cu–CeTi exhibiting the lowest value at 3.13 eV. Also, more copper resulted in higher absorption in the entire visible range, together with the appearance of the broad absorption band located between 500 and 600 nm (Figure 6C–E). This band is a signature response of the LSPR of metallic copper NPs [16].

Photoluminescence (PL) can be used as an indicator for emissive hot carrier recombination, which acts detrimentally for photocatalytic reactions. Because of electron–hole recombination and light emission upon thermalization, hot carriers cannot participate in the light-driven catalytic reaction [47]. The PL spectrum of the $CeO_2$ support shows several bands in the energy range between 2.9 and 2.3 eV, which is characteristic of electron-hole recombination across the bandgap and from the electron trapping states below the conduction band minimum, Figure 6G,H. For the CeTi support, the PL intensity and thus recombination in the 2.9–2.7 eV range is notably diminished compared to pure $CeO_2$, revealing that titanium doping produces defect sites, which act as electron trapping sites and prevent recombination from the CB and shallow trap states. With deposition of copper, PL intensity progressively decreases, which originates from hot electron mobility to copper and attenuation of recombination, likely because of Schottky barrier formation at the interface [48]. Consequently, doping of ceria with titanium and subsequent copper deposition progressively diminishes emissive carrier recombination, thus increasing the availability of more excited charge carriers for the light-assisted reaction.

## 2.4 | DRIFT Spectroscopy

We first analyzed the effect of light on the surface species during steady-state RWGS reaction conditions (Figure 7A–D). Reaction temperature and total reactant flow were maintained constant, and the CO formation rate was manipulated by changing the $H_2/CO_2$ ratio in the feed.

Increasing the copper content in the catalysts led to a progressive decrease of all IR-active species, thus confirming previous studies that they populate primarily the ceria surface [25]. Under dark RWGS conditions (black traces in Figure 7), an excess of hydrogen resulted in accelerated CO rate and IR band attenuation in the broad range between 1000 and 1550 $cm^{-1}$, where the C–O vibrations of different carbonate species occur. The C–H band of formates (2845 $cm^{-1}$) remained largely unaffected.

Contrarily, under light-assisted conditions, excess hydrogen diminished the CO formation rate for all tested copper loadings. This is in line with the negative $H_2$ reaction orders that were identified during kinetic analysis (Figure 3) and highlights very different reaction channels occurring under dark and illuminated conditions. Under illuminated RWGS reaction conditions, the intensity of all surface species is lower compared to identical conditions under dark, revealing a less populated catalytic surface. Progressively increasing the $CO_2$ fraction in the feed increases the CO rate, and the spectral changes manifest themselves mainly by decreasing the formate C–H (2845 $cm^{-1}$) and $\nu(OCO)_{asym}$ (1585 $cm^{-1}$) band intensities.

With transient DRIFT experiments, we further analyzed the extent of decay of formate and carbonate species after the $CO_2 + H_2 \rightarrow H_2$ step change, Figure 8 and Figures S8–S10. The effect of titanium doping (3Cu–CeTi vs. 3Cu–Ce) and copper loading (3Cu–CeTi vs. 30Cu–CeTi) is compared. Results are presented in two wavenumber regions: 3100–2700 $cm^{-1}$ (Figure 8A,C) for

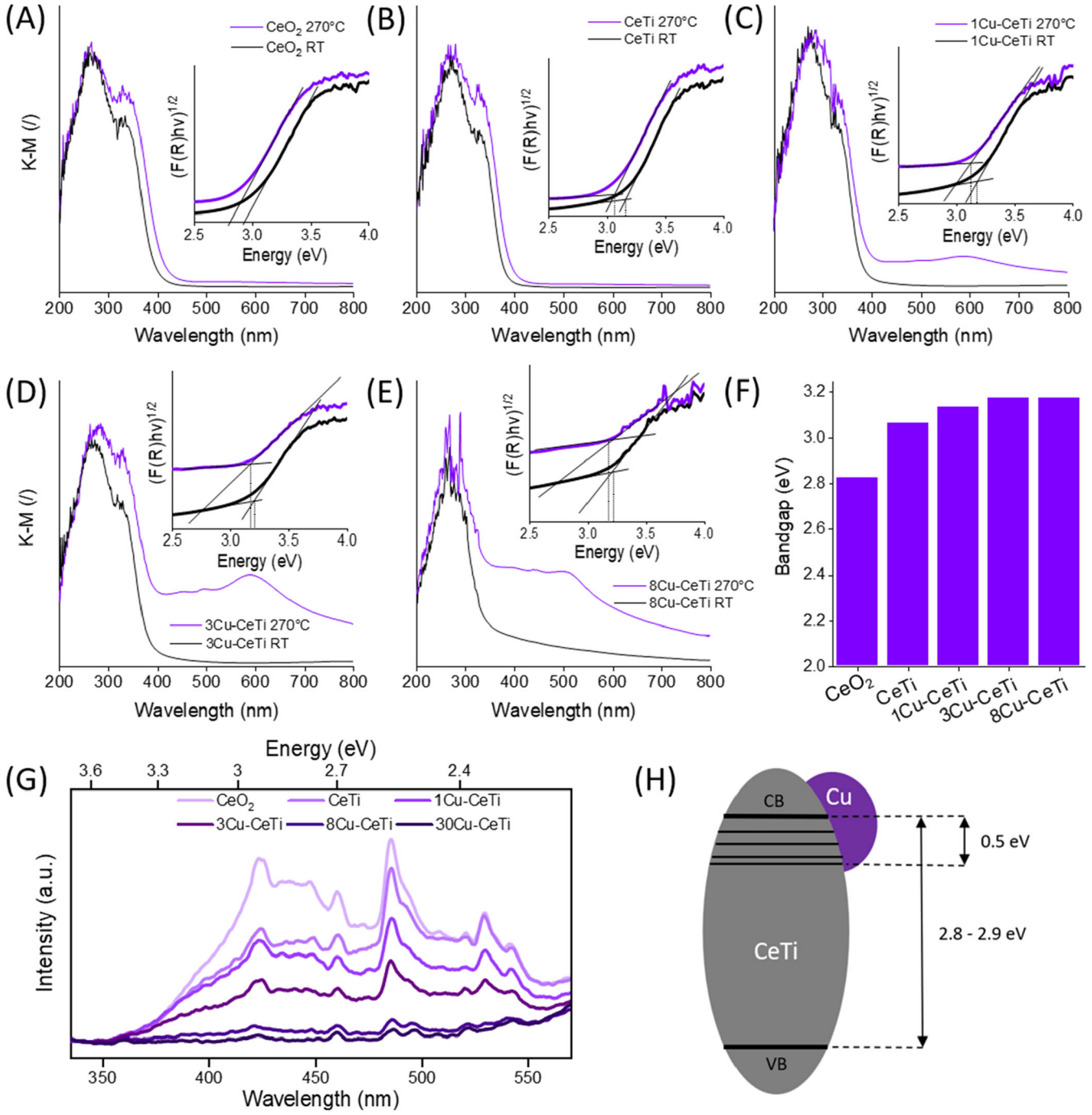


**FIGURE 6** | UV–Vis DR spectra of (A) bare $CeO_2$, (B) $CeTiO_2$ nanorods, (C) 1Cu–CeTi, (D) 3Cu–CeTi, and (E) 8Cu–CeTi measured at RT in air (black) and at 270°C in $H_2/CO_2$ flow (violet). The flow of the inlet gas feed was constant at 30 mL $min^{-1}$. Insets show Tauc plots to determine the indirect bandgap values. Results for the 30Cu–CeTi sample are not shown because of the black sample color and total absorbance in the entire spectral range. (F) Optical bandgap value comparison under RWGS reaction conditions. (G) Photoluminescence spectra and (H) schematic representation of the copper–ceria contact and trap states within the bandgap of the CeTi support.

C–H vibrations, and 1900–800 $cm^{-1}$ (Figure 8B,D) for OCO as well as C=O vibrations of both formate and carbonate species. Before the step change, under both dark- and light-assisted conditions ($t = 0$, Figure 8), the characteristic symmetric and asymmetric C–H vibrations (2950–2800 $cm^{-1}$) coexist with the OCO stretching (1585 $cm^{-1}$), corresponding to the presence of monodentate and bidentate formate species [25]. In the region between 1650 and 1000 $cm^{-1}$, several other bands of different carbonates are also observed: monodentate (M, 1495 $cm^{-1}$), bidentate (B, 1292 $cm^{-1}$), and polydentate (P, 1370 $cm^{-1}$). It must be emphasized that the P carbonate band at 1370 $cm^{-1}$ overlaps with the symmetric OCO vibration of bidentate formate [49, 50].

The signals over the 3Cu–CeTi (Figure 8) and 3Cu–Ce catalyst appear very similar (Figure S9), revealing a minor role of titanium dopant on the most abundant surface species. However, when copper content is increased from 3 to 30 wt.%, the abundance of surface species notably decreases, as can be

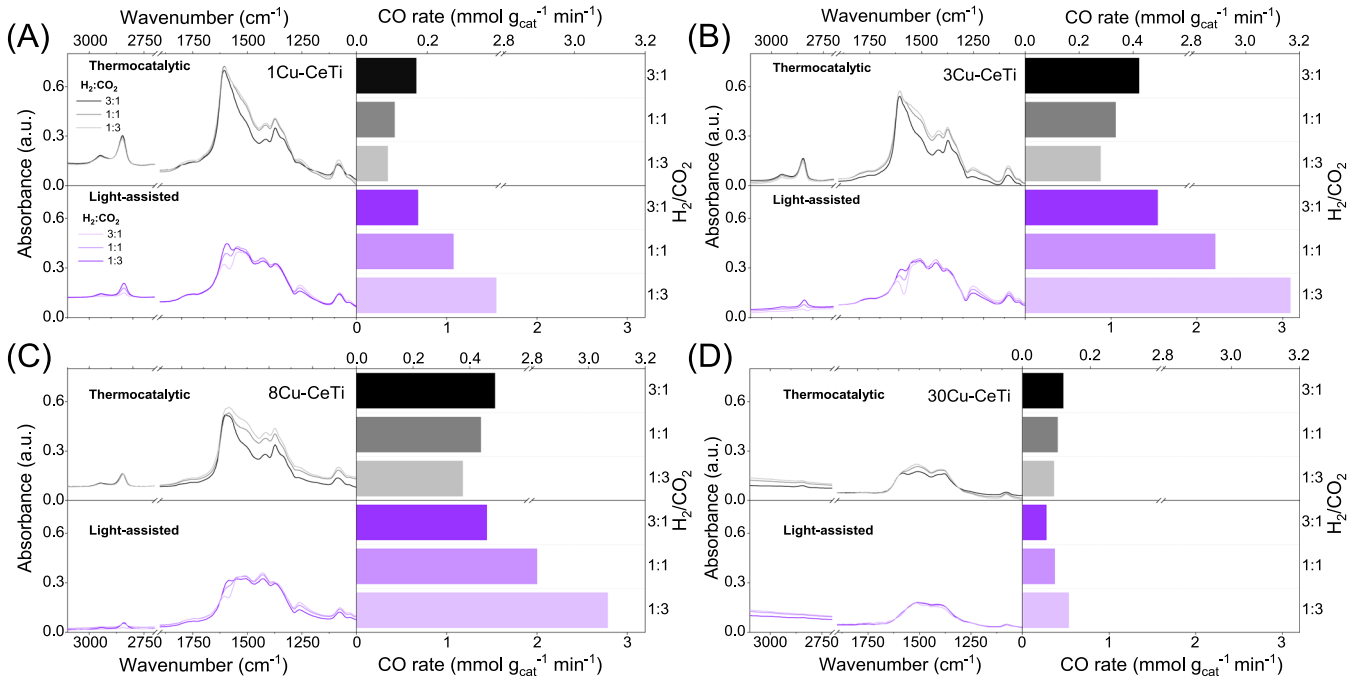


**FIGURE 7** | (A–D) *Operando* DRIFT spectra and the corresponding CO rates for the Cu–CeTi catalysts containing 1, 3, 8, and 30 wt.% copper during steady-state thermocatalytic and light-assisted RWGS conditions. All these experiments were done at a constant temperature of 300°C and 15 mL $min^{-1}$ of various $H_2/CO_2$ gas ratios. During the light-assisted reaction, the sample was irradiated by 1.58 W $cm^{-2}$ of visible light.

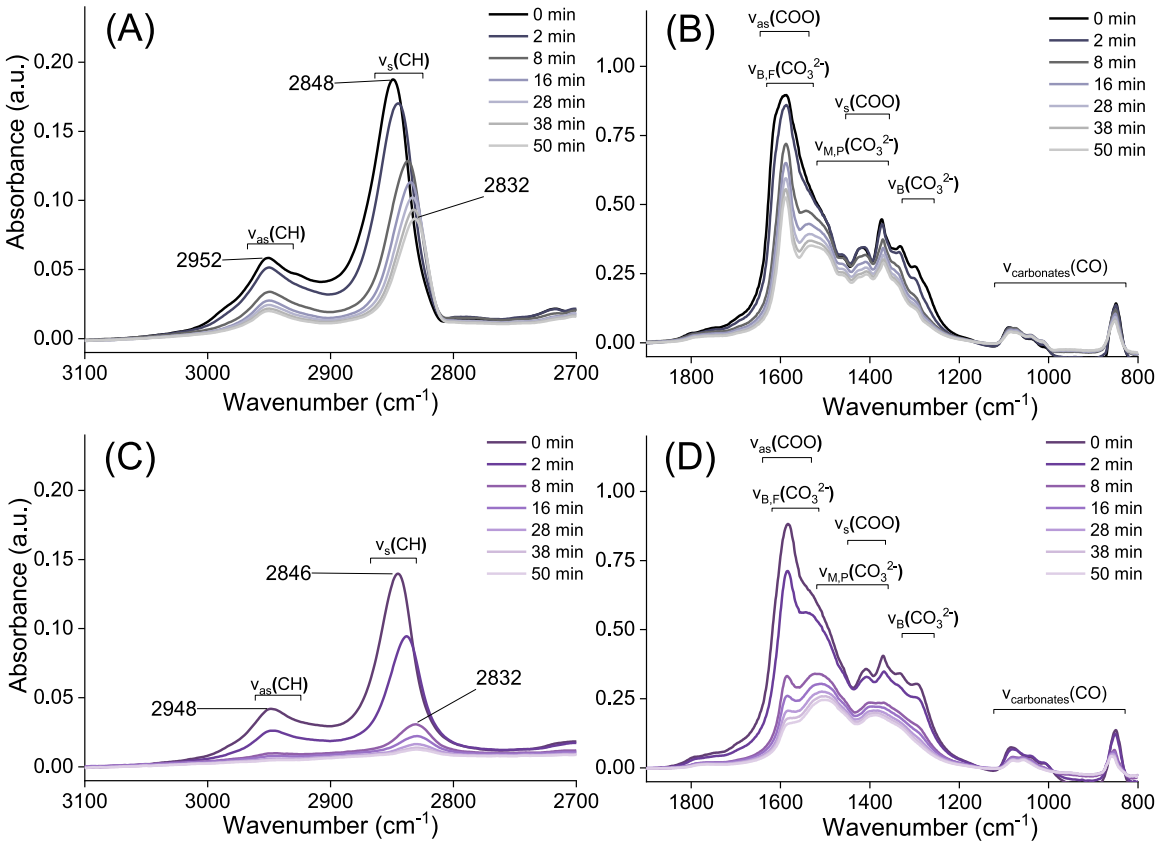


**FIGURE 8** | (A, B) DRIFT spectra of the 3Cu–CeTi catalyst at 270°C under RWGS conditions during thermal and (C, D) light-assisted conditions showing the evolution of surface species after the $CO_2 + H_2 \rightarrow H_2$ step change. The $H_2 + CO_2 \rightarrow CO_2$ switch was performed at 270°C, and irradiance of 230 mW $cm^{-2}$ was used during the light-assisted reaction. The total flow rate of 30 mL $min^{-1}$ was used ($H_2/CO_2 = 1$).

concluded from about 3 times lower peak intensities in the 1200–1800 $cm^{-1}$ region and about 7 times lower formate band intensity at 2845 $cm^{-1}$, Figures 8 and S9.

After the $CO_2 + H_2 \rightarrow H_2$ step change in the dark, the intensity of all peaks decreases (Figure 8A,B). The initial signal intensity decays by about 60% for the COO (1585, 1340 $cm^{-1}$) and C–H (2950, 2845 $cm^{-1}$) bands of formate species. Also, the $\upsilon_s$(CH) peak frequency redshifts with time from 2848 to 2832 $cm^{-1}$, which suggests that initially two types of formates are present: bidentate (BF) and monodentate (MF). Mudiyanselage et al. assigned these vibrations to bidentate and monodentate formate species using IRRAS on inverse $CeO_x$–$Cu_yO$/Cu(1 1 1) model systems [51]. The decrease of OCO bands, assigned to M, B, and P carbonates (1495, 1292, and 1370 $cm^{-1}$) is 27%, 60%, and 34% in 50 min.

Under visible light illumination (Figure 8C,D), the intensity of all surface species drops more extensively within the monitored 50 min interval compared to the experiment in the dark. Namely, the C–H vibrations assigned to MF and BF (2846 and 2832 $cm^{-1}$) are completely attenuated, while M, B, and P carbonate species (1495, 1292, and 1370 $cm^{-1}$) lose 52%, 73%, and 56% of initial intensity, respectively.

Finally, we compared the initial intensity decay rates for the most abundant surface species (formate, as well as polydentate and bidentate carbonate), with the aim to identify which species gain the most in reactivity by illumination [52]. Due to substantial overlap of the C–O band vibrations originating from carbonate and formate species, some decay rates are reported as lumped values (Table 1). The initial decay rate of characteristic carbonates and formates on the illuminated catalysts is 1.5- to 4.2-fold higher compared to dark conditions, which reveals a positive effect of light on their removal and, consequently, their increased reactivity.

The decay of the formate (BF) band is 1.5 and 1.7 times higher under illumination for the 3Cu–CeTi and 3Cu–$CeO_2$ samples, but notably slower (0.4) for the 30Cu–CeTi sample. This indicates intrinsically different reactivity of formates, which depends on the chemistry of the binding site (bulk Cu, Cu–$CeO_{2-x}$ interface, or $CeO_{2-x}$) [51, 53].

The bidentate and polydentate carbonates (B and P) decay between 4.2 and 3.2 times faster under illumination for the 3Cu–$CeO_2$ and 3Cu–CeTi samples, revealing that the carbonate removal is accelerated more compared to formate. The polydentate carbonate is less reactive compared to the bidentate because of its stronger bonding to the surface via forming one Ce–O and two $O_{surf}$–C interactions [23].

## 3 | Discussion

Illumination of the 3Cu–CeTi catalyst with 770 mW $cm^{-2}$ of visible light has several notable and beneficial consequences on RWGS activity: (i) accelerates the CO rate up to 57 times compared to reaction in the dark at 210°C, (ii) decreases the $E_a$ values from 92 to 26 kJ $mol^{-1}$, (iii) the apparent reaction order with respect to $H_2$ changes from 1 to −0.6, and (iv) selectivity to

**TABLE 1** | Initial decay rates for the most abundant surface species. Bidentate formate (BF), $\nu_{as}$(CH), 2845 $cm^{-1}$; bidentate carbonate and bidentate carbonate (B + BF), $\nu_{as}$(COO), 1585 $cm^{-1}$; polydentate carbonate and bidentate formate (P + BF), $\nu_s$(COO), 1370 $cm^{-1}$; polydentate carbonate (P), $\nu$(CO), 1085 $cm^{-1}$; and bidentate carbonate (B), $\nu$(CO), 850 $cm^{-1}$. Dark and bright symbols present the dark- and light-assisted intensity trends, respectively.

| Surface species, wavenumber ($cm^{-1}$) | 3Cu–CeTi | | | 3Cu–$CeO_2$ | | | 30Cu–CeTi | | |
|---|---|---|---|---|---|---|---|---|---|
| | Rate light ($10^{-4}$ $s^{-1}$) | Rate dark ($10^{-4}$ $s^{-1}$) | Ratio light/dark | Rate light ($10^{-4}$ $s^{-1}$) | Rate dark ($10^{-4}$ $s^{-1}$) | Ratio light/dark | Rate light ($10^{-4}$ $s^{-1}$) | Rate dark ($10^{-4}$ $s^{-1}$) | Ratio light/dark |
| BF, 2845 | −4.4 ± 0.1 | −2.9 ± 0.1 | 1.5 ± 0.2 | −7.0 ± 0.2 | −4.1 ± 0.1 | 1.7 ± 0.2 | −0.2 ± 0.1 | −0.5 ± 0.1 | 0.4 ± 0.1 |
| B + BF, 1585 | −17.9 ± 0.7 | −4.5 ± 0.2 | 4.0 ± 0.3 | −15 ± 0.6 | −5.0 ± 0.2 | 3.0 ± 0.2 | −3.5 ± 0.3 | −1.7 ± 0.1 | 2.2 ± 0.2 |
| P + BF, 1370 | −6.0 ± 0.3 | −2.0 ± 0.1 | 3.0 ± 0.2 | −4.1 ± 0.5 | −1.4 ± 0.1 | 2.9 ± 0.6 | −2.3 ± 0.2 | −0.6 ± 0.1 | 3.8 ± 1.0 |
| P, 1085 | −1.5 ± 0.1 | −0.5 ± 0.1 | 3.2 ± 0.4 | −2.5 ± 0.1 | −0.8 ± 0.2 | 3.3 ± 0.3 | −0.8 ± 0.1 | −0.3 ± 0.1 | 2.2 ± 0.7 |
| B, 850 | −3.0 ± 0.2 | −0.9 ± 0.1 | 3.5 ± 0.5 | −5.5 ± 0.2 | −1.3 ± 0.1 | 4.2 ± 0.3 | −2.1 ± 0.2 | −0.6 ± 0.1 | 3.8 ± 0.9 |

methane under $H_2$ excess feed is totally attenuated. This reveals that the reaction mechanism is substantially altered upon illumination. Also, the surface coverage with hydrogen is fivefold higher during illumination compared to the dark, which makes surplus of hydrogen in the feed, which is traditionally used in thermocatalysis to increase $CO_2$ conversion, redundant in the light-assisted RWGS reaction.

The combination of $H_2$-TPR, $H_2$-TPD, and in situ UV–Vis characterization results reveals that 20% of $Ce^{4+}$ transforms to $Ce^{3+}$ during the catalyst activation step, which shifts the light absorption of substoichiometric ceria into the visible range [21, 33]. Copper is reduced to a metallic state and, as such, is present during the RWGS reaction, thus exhibiting strong absorption in the visible range of the light spectrum and enabling LSPR excitation upon illumination [5].

Raman spectroscopy showed that a copper loading of 3 wt.% induces structural changes in the ceria support. The Frenkel-type oxygen dislocations are eliminated, and oxygen vacancies are formed, likely due to copper ($Cu^{2+}$) embedding into the ceria structure. The 75% copper dispersion of the 3Cu–CeTi sample, with a corresponding copper particle diameter of 1.5 nm (Table S4), together with the presence of oxygen vacancies in ceria, ensures the abundance of $Cu–O_v–Ce^{3+}$ interfacial active sites.

Titanium modification of the ceria support does not shrink the bandgap values nor influences the amount of achievable $Ce^{3+}$, but rather diminishes emissive recombination from the electron trap levels just below the conduction band. This enables more efficient hot carrier utilization to drive the light-assisted RWGS reaction.

The *operando* steady-state DRIFT results suggest that the primary active sites for $CO_2$ chemisorption (in the form of $CO_3$* and HCOO* species) are located on the $CeTiO_2$ support. The role of copper is to adsorb $H_2$, facilitate its dissociation, and enable hydrogenation at the copper-support interface [5, 31]. All catalysts are less densely populated with carbon-containing species during illumination, suggesting that light causes their destabilization and increases their reactivity. The CO rate increases with decreasing carbonate and formate population, suggesting their important role in CO formation during the light-assisted RWGS reaction.

Our transient in situ DRIFTS experiments showed that formates are completely removed from the catalyst's surface under illumination, whereas they lose only about 60% of the initial population in the dark. As a result, illumination turns the inactive monodentate formate spectators into reaction intermediates.

The comparison of initial decay rates provided direct information on the reactivity of different surface species. Reactivity of formates is increased during illumination by 1.5- to 1.7-fold compared to dark on the 3Cu–CeTi catalyst, which contains the average copper size of 1.5 nm. However, as the copper size increases to 18 nm (30Cu–CeTi sample), the formates become more stable during illumination. Such structure-sensitivity is manifested through vastly different $E_a$ values under illumination (26 and 57 kJ $mol^{-1}$ for 3Cu–CeTi and 30Cu–CeTi, respectively) and suggests that the reactivity of formates is influenced by their position (residing on bulk-like copper or ceria) and is accelerated by oxidation with hot holes, generated on the photoexcited ceria [33]. As a result, the beneficial effect of light on the formate reactivity is achieved on samples with high copper dispersion and the absence of bulk copper. Despite the formates showing higher stability upon illumination, the catalyst 30Cu–CeTi exhibited substantial CO rate acceleration during illumination, which proves there is another kinetically relevant reaction channel that produces CO. Since the redox reaction mechanism does not contribute to CO formation under the reaction conditions of this work (no CO generation was detected after pulsing $CO_2$ over the reduced catalyst), the remaining species must be carbonates. The light-induced reactivity of bidentate and polydentate carbonates ranges from 3.2 to 4.2, which is about twice the value of formates. The full benefit of light in the RWGS reaction activity is achieved when both copper and substoichiometric ceria catalytic components are photoexcited simultaneously.

Upon illumination of Cu moieties, the Cu LSPR is triggered. With electromagnetic nearfield enhancement around copper, rotational and vibrational energy is transferred into the adsorbed species residing on the Cu and its intimate proximity (up to a couple of nm), thus weakening their bonds and increasing reactivity [21, 54]. As a result, a lower energy barrier must be overcome by thermal effects (heating), and the activation barrier for reaction steps at the $Cu–CeTiO_2$ interface is expected to decrease. This correlates with the macroscopically observed decrease in the $E_a$ values under illumination.

The bandgap excitation of ceria triggers photoexcited hot electrons and hot holes. Hot electrons facilitate the $CO_2$ activation process, which occurs via electron injection into the $CO_2$ molecule, forming a bent $CO_2^-$ anion [55]. The electron transfer process is the rate-limiting step for $CO_2$ dissociation over ceria-based materials [56] and is likely also related to the linear scaling between the irradiance and reaction rate. However, $CO_2$ dissociation does not proceed without the involvement of H species.

Hot holes can participate in the reaction with surface oxide species ($O^{2-}$) originating from hydroxyl species decomposition (Figure S11 and Supporting Information), and fill the oxygen vacancy sites, causing ceria reoxidation. The oxidized ceria surface is crucial for hosting formate and carbonate species, which are bound to the surface via “surface lattice” oxygen atoms [57].

This way, the carbonate species, which populate the ceria surface, can react more swiftly with the abundant hydrogen species originating from photoexcited copper, thus facilitating both accelerated carbonate conversion to formate, and further formate decomposition to CO ($HCOO^* \rightarrow CO_{(g)} + OH^*$, followed by $^*OH + H^* \rightarrow H_2O + 2^*$). Upon catalyst illumination with blue light ($\lambda = 400–450$ nm), the AQY value reached 1.6%. This is substantially more compared to the AQY value of 1.1%, which was achieved with selective photo excitation of only copper LSPR. The reaction channels contributing to CO formation include cooperative participation of both copper and ceria phases, as well as $H_2$ and $CO_2$-based reaction intermediates.

## 4 | Conclusions

This study demonstrates the positive impact of visible light on the activity of copper/ceria catalysts in the RWGS reaction. Small copper loading (i.e., 3 wt.%) produces the most active photocatalyst, which contains nanometer-sized copper particles dispersed on the partly reduced ceria support, resulting in the abundant $Cu–O^{v}–Ce^{3+}$ reactive interfacial sites. The reaction orders, $E_a$, and wavelength-dependent CO rate suggest that the improved catalyst reactivity under illumination has a light-induced origin. Simultaneous photoexcitation of copper and ceria phases activates the spatially segregated reaction intermediates (HCOO* and $CO_3$* on ceria support, H* on copper), which enables efficient photon utilization to drive the photocatalytic $CO_2$ hydrogenation under mild conditions, unattainable with thermal catalyst excitation. Hydrogen dissociation is greatly improved upon illumination, which enables the use of equimolar $H_2/CO_2$ or $CO_2$-rich feed streams for maximal CO rates. The cumulative effect of simultaneous Cu and $CeTiO_{2-x}$ phase photoexcitation results in a drastic acceleration of the RWGS rate and a strong decrease of the $E_a$ values. Considering the $CO_2$ reaction order under illumination increases notably ($0.36 \rightarrow 0.75$), while that for $H_2$ assumes a negative value, the RDS under the light-assisted conditions is likely related to abundance of surface adsorbed $CO_2$ and $CO_2$ reactivity, either through the formate generation step ($CO_2 + H \rightarrow HCOO$), carbonate decomposition step ($CO_3^* + H^* \rightarrow HCOO^* + O^*$), or carboxylate species formation through altered hydroxyl reactivity.

## 5 | Materials and Methods

*Catalyst synthesis*—Bare $CeO_2$ nanorods and $CeO_2$ nanorods modified with titanium were synthesized by dissolving 58.8 g of NaOH (Merck, purity 99%) in 140 mL ultrapure water. For Ti modification, 73 μL of $Ti[OCH(CH_4)_2]_4$ (Aldrich, purity 97%) was added and dissolved in this solution, respectively. Then, a separate 84 mL aqueous solution containing 4.9 g of $Ce(NO_3)_3{\cdot}6H_2O$ (Sigma Aldrich, purity 99%) was added under vigorous stirring in both cases. The suspensions were stirred for 30 min and transferred into Teflon-lined stainless-steel autoclaves (35 mL volume). The autoclaves were heated to 100°C for 24 h. After cooling to room temperature, the suspension was centrifuged at 7500 rpm for 3 min and washed several times using ultrapure water and absolute ethanol until all sodium was removed from the precipitate. The obtained solids were freeze-dried and then calcined in static air at 500°C (5°C $min^{-1}$ heating ramp) for 4 h.

The deposition precipitation method was used to disperse 1, 3, and 8 wt.% of copper. First, 15.4, 47, or 123 mg of $Cu(NO_3)_3{\cdot}3H_2O$ was dissolved in 40 mL of ultrapure water, and then 400 mg of the ceria support was added and stirred for 20 min. Afterward, 25 wt.% ammonia solution was added dropwise until the pH of the solution reached 9. In the span of 3 h under stirring, 150 mL of ultrapure water was added dropwise, followed by centrifugation at 9000 rpm for 2 min. Because the deposition precipitation method is poorly suited for higher metal loadings, the incipient wetness impregnation method was used to deposit 30 wt.% of copper; 652 mg of $Cu(NO_3)_3{\cdot}3H_2O$ (Fluka, purity 99%) was dissolved in 0.4 mL of ultrapure water. The solution was poured over 400 mg of ceria support and mixed until fully homogenized. All containing Cu samples were dried at 80°C (5°C $min^{-1}$) for 5 h, followed by calcination in air at 350°C (2°C $min^{-1}$) for 3 h.

The synthesized catalysts are denoted as *x*Cu–Ce and *x*Cu–CeTi for pure and titanium-modified $CeO_2$ nanorods, respectively. Letter *x* represents the nominal copper content.

*XRD analysis* was performed on Panalytical XP PRO MPD apparatus using $Cu_{\alpha 1}$ irradiation ($\lambda = 1.5406$ Å) in the $2\theta$ range between 20°and 80°, step size of 0.034°, and fully opened 100 channel X′ Celerator detector. Rietveld refinement was applied to calculate the lattice parameters of $CeO_2$.

*$N_2$ physisorption analysis* (Tristar II apparatus from Micromeritics) was used to calculate specific surface area, total pore volume, and average pore size (BJH method) of the synthesized materials. Specific surface area was determined using the BET method in the relative pressure range up to 0.3 $p/p_o$, and the total pore volume was determined from the $N_2$ adsorption isotherm at $p/p_0 \approx 0.95$, assuming complete pore filling. Before analysis, samples were degassed for 1 h at 90°C, followed by 4 h at 300°C in $N_2$ flow (purity 6.0, Linde) using a SmartPrep accessory (Micromeritics).

*Microscopy*—Morphology of the prepared catalysts was studied using a field-emission scanning electron microscope (Carl Zeiss, FE-SEM SUPRA 35VP), equipped with energy-dispersive X-ray spectroscopy hardware (Oxford Instruments, model INCA 400). TEM visualization was performed by a scanning transmission electron microscope, JEOL ARM 200 CF.

*Raman spectroscopy* was performed on a WiTec Alpha 300 RA spectrometer using a 532 nm laser and a 50× objective, 4 s integration time, and 20 accumulations per scan.

*UV–Vis DR spectroscopy*—In situ UV–Vis diffuse reflectance (UV–Vis DR) analysis (Lambda 650 apparatus by Perkin Elmer) was conducted using 10 mg of the powdered catalysts, loaded into the Harrick reaction chamber. Spectra were recorded between 850 and 200 nm with a scan speed of 90 nm $min^{-1}$. Spectralon was used for background correction. Samples were analyzed at room temperature (22°C ± 1°C, RT) in air, and at 270°C in equimolar $H_2/CO_2$ flow (30 mL $min^{-1}$). PL spectra were recorded on the LS55 spectrometer by Perkin Elmer with a 300 nm excitation wavelength at ambient conditions.

*DRIFTS analysis* was performed with 10 mg of powdered catalyst, which was loaded into the Harrick reaction chamber. Spectra were recorded between 800 and 4000 $cm^{-1}$ with 32 accumulations per scan and a spectral resolution of 4 $cm^{-1}$. The samples were initially reduced in $H_2$/Ar flow (10 and 20 mL $min^{-1}$, respectively) at 320°C for 30 min. At this point, the background was recorded with the activated sample. For the steady-state experiments, the temperature decreased to 300°C and the total flow rate was maintained at 15 mL $min^{-1}$. $H_2/CO_2$ feed ratio was varied stepwise: 3:1, 1:1, and 1:3. During the light-assisted reaction, the sample was irradiated by visible light (1.58 W $cm^{-2}$). The high temperature and irradiance were used to maximize the catalytic activity differences under different dark and illuminated

conditions. The reaction products were analyzed by a micro-GC (Agilent490), connected online to the reaction chamber.

For the transient step-change experiment, the sample pretreatment and spectral acquisition conditions were identical to those above. The $H_2 + CO_2 \rightarrow CO_2$ switch was performed at 270°C and irradiance of 230 mW cm$^{-2}$. The total flow rate of 30 mL min$^{-1}$ was used ($H_2/CO_2 = 1$), and the switch was made by a manually actuated 4-way Vici valve. Lower reaction temperature and irradiance were used to capture the peak decay dynamics more accurately, since the spectral acquisition was performed with a time resolution of about 17 s.

*Catalytic tests* were conducted in a Harrick reaction chamber in the temperature range of 210°C–320°C. During the light-assisted experiments, the catalysts were illuminated with white light, while the catalyst temperature was varied by adjusting the power of the electric heater. The illumination of the catalysts was constant and provided by a Schott KL2500 LED source (visible light; $\lambda = 400–700$ nm), equipped with an optic fiber having a 9 mm active diameter. The power of light, measured by the Thorlabs PM100D photometer, was 770 mW cm$^{-2}$. For the reaction, 10 mg of finely powdered catalyst was placed in the reaction chamber, forming a catalyst layer with a diameter of 6.4 mm and a thickness of 0.5 mm. Under the catalyst layer, 25 mg of SiC powder was placed to improve heat transfer to and from the catalyst layer. To ensure accurate monitoring of the catalyst bed temperature, a thermocouple was positioned in the center so that it contacted the underside of the illuminated catalyst layer, Figure S12. For the preliminary assessment of catalytic activity, different $H_2/CO_2$ feed ratios (2.4/1 or 1/1) were tested, with a total flow of 30 mL min$^{-1}$. During the wavelength-dependent studies, different bandpass filters were used (400–450 nm, 450–550 nm, 550–600 nm, and 600–700 nm, and irradiance was maintained constant at 230 mW cm$^{-2}$). Kinetic analysis was performed at 270°C, the catalyst was irradiated by 770 mW cm$^{-2}$ of white light, the total flow rate was 40 mL min$^{-1}$, and the mass of the catalyst was 10 mg. Outlet gas was analyzed by GC (model 490 by Agilent, equipped with MS5A and PPU columns).


## Acknowledgments

Slovenian Research and Innovation Agency (ARIS) financed this research through projects N2-0265 and P1-0418. Mojca Opresnik, Edi Kranjc, and Prof. Dr. Goran Dražić are kindly acknowledged for SEM, XRD, and TEM analyses. Dr. Matej Bubaš is acknowledged for inspiring scientific discussions. Andrej Race from the Materials Chemistry Department at NIC is kindly acknowledged for recording the Raman spectra.


## Conflicts of Interest

The authors declare no conflicts of interest.

## References


1. H. Ritchie, P. Rosado, and M. Roser, "$CO_2$ and Greenhouse Gas Emissions," 2023, https://ourworldindata.org/co2-and-greenhouse-gas-emissions.

2. D. Mateo, J.-L. Cerrillo, S. Durini, and J. Gascon, "Fundamentals and Applications of Photo-Thermal Catalysis," *Chemical Society Reviews* 50, no. 3 (2021): 2173–2210.

3. Q. Bi, K. Hu, J. Chen, et al., "Black Phosphorus Coupled Black Titania Nanocomposites With Enhanced Sunlight Absorption Properties for Efficient Photocatalytic $Co_2$ Reduction," *Applied Catalysis, B: Environmental* 295 (2021): 120211.

4. Y. Qi, J. Jiang, X. Liang, et al., "Fabrication of Black $In_2O_3$ With Dense Oxygen Vacancy Through Dual Functional Carbon Doping for Enhancing Photothermal $CO_2$ Hydrogenation," *Advanced Functional Materials* 31, no. 22 (2021): 2100908.

5. L. Lin, S. Yao, Z. Liu, et al., "In Situ Characterization of Cu/$CeO_2$ Nanocatalysts for $CO_2$ Hydrogenation: Morphological Effects of Nanostructured Ceria on the Catalytic Activity," *Journal of Physical Chemistry C* 122, no. 24 (2018): 12934–12943.

6. A. Santoro, A. M. Cancelliere, K. Kamogawa, et al., "Photocatalyzed $CO_2$ Reduction to CO by Supramolecular Photocatalysts Made of Ru(II) Photosensitizers and Re(I) Catalytic Subunits Containing Preformed $CO_2$TEOA Adducts," *Scientific Reports* 13, no. 1 (2023): 11320.

7. J. Volders, K. Elen, A. Raes, et al., "Sunlight-Powered Reverse Water Gas Shift Reaction Catalysed by Plasmonic Au/$TiO_2$ Nanocatalysts: Effects of Au Particle Size on the Activity and Selectivity," *Nanomaterials* 12, no. 23 (2022): 4153.

8. P. Kaiser, R.-B. Unde, C. Kern, and A. Jess, "Production of Liquid Hydrocarbons With $CO_2$ as Carbon Source Based on Reverse Water-Gas Shift and Fischer–Tropsch Synthesis," *Chemie Ingenieur Technik* 85, no. 4 (2013): 489–499.

9. K. Lorber and P. Djinović, "Accelerating Photo-Thermal $CO_2$ Reduction to CO, $CH_4$ or Methanol Over Metal/Oxide Semiconductor Catalysts," *iScience* 25, no. 4 (2022): 104107.

10. F. Fresno, A. Iglesias-Juez, and J.-M. Coronado, "Photothermal Catalytic $CO_2$ Conversion: Beyond Catalysis and Photocatalysis," *Topics in Current Chemistry* 381, no. 4 (2023): 21.

11. X. Li, J. Yu, M. Jaroniec, and X. Chen, "Cocatalysts for Selective Photoreduction of $CO_2$ Into Solar Fuels," *Chemical Reviews* 119, no. 6 (2019): 3962–4179.

12. S. Fang and Y.-H. Hu, "Thermo-Photo Catalysis: A Whole Greater Than the Sum of Its Parts," *Chemical Society Reviews* 51, no. 9 (2022): 3609–3647.

13. X. Chen, Y. Zhao, J. Han, and Y. Bu, "Copper-Based Catalysts for Electrochemical Reduction of Carbon Dioxide to Ethylene," *ChemPlusChem* 88, no. 1 (2023): e202200370.

14. Y.-F. Shi, S. Ma, and Z.-P. Liu, "Copper-Based Catalysts for $CO_2$ Hydrogenation: A Perspective on Active Sites," *EES Catalysis* 1, no. 6 (2023): 921–933.

15. P. Ebrahimi, A. Kumar, and M. Khraisheh, "Combustion Synthesis of Copper Ceria Solid Solution for $CO_2$ Conversion to CO via Reverse Water Gas Shift Reaction," *International Journal of Hydrogen Energy* 47, no. 97 (2022): 41259–41267.

16. P. Liu, H. Wang, X. Li, M. Rui, and H. Zeng, "Localized Surface Plasmon Resonance of Cu Nanoparticles by Laser Ablation in Liquid Media," *RSC Advances* 5, no. 97 (2015): 79738–79745.

17. Y. Fang, Z. Cheng, S. Wang, et al., "Effects of Oxidation on the Localized Surface Plasmon Resonance of Cu Nanoparticles Fabricated via Vacuum Coating," *Vacuum* 184 (2021): 109965.

18. K. Chang, H. Zhang, M. Cheng, and Q. Lu, "Application of Ceria in $CO_2$ Conversion Catalysis," *ACS Catalysis* 10, no. 1 (2020): 613–631.

19. X. Han, L. Jiang, Z. Zhang, et al., ""Photothermal-Enhanced Anti-$SO_2$ Performance of a $MoWO_x$/$CeO_2$ Catalyst in Low-Temperature $NH_3$-SCR," *Environmental Science & Technology* 59, no. 24 (2025): 12364–12377.

20. B. Deng, H. Song, K. Peng, Q. Li, and J. Ye, "Metal-Organic Framework-Derived Ga–Cu/$CeO_2$ Catalyst for Highly Efficient Photothermal Catalytic $CO_2$ Reduction," *Applied Catalysis, B: Environmental* 298 (2021): 120519.

21. K. Lorber, J. Zavašnik, J. Sancho-Parramon, M. Bubaš, M. Mazaj, and P. Djinović, "On the Mechanism of Visible-Light Accelerated Methane Dry Reforming Reaction Over Ni/$CeO_{2-x}$ Catalysts," *Applied Catalysis, B: Environmental* 301 (2022): 120745.

22. P. Ebrahimi, A. Kumar, and M. Khraisheh, "A Review of $CeO_2$ Supported Catalysts for $CO_2$ Reduction to CO Through the Reverse Water Gas Shift Reaction," *Catalysts* 12, no. 10 (2022): 1101.

23. A. Trovarelli, "Catalytic Properties of Ceria and $CeO_2$-Containing Materials," *Catalysis Reviews* 38, no. 4 (1996): 439–520.

24. A. Trovarelli and J. Llorca, "Ceria Catalysts at Nanoscale: How Do Crystal Shapes Shape Catalysis?," *ACS Catalysis* 7, no. 7 (2017): 4716–4735.

25. K. Lorber, J. Zavašnik, I. Arčon, et al., "$CO_2$ Activation Over Nanoshaped $CeO_2$ Decorated With Nickel for Low-Temperature Methane Dry Reforming," *ACS Applied Materials & Interfaces* 14, no. 28 (2022): 31862–31878.

26. Y. Wang, Y. Zhao, S. Zhu, et al., "Insight Into the Effect of $CeO_2$ Morphology on Catalytic Performance for Steam Reforming of Glycerol," *Fuel* 334, Part 1 (2023): 126587.

27. A.-D. Liyanage, S.-D. Perera, K. Tan, Y. Chabal, and K.-J. Balkus, "Synthesis, Characterization, and Photocatalytic Activity of Y-Doped $CeO_2$ Nanorods," *ACS Catalysis* 4, no. 2 (2014): 577–584.

28. D.-P.-H. Tran, M.-T. Pham, X.-T. Bui, Y.-F. Wang, and S.-J. You, "$CeO_2$ as a Photocatalytic Material for $CO_2$ Conversion: A Review," *Solar Energy* 240 (2022): 443–466.

29. S.-M. Lee, H. Eom, and S. S. Kim, "A Study on the Effect of $CeO_2$ Addition to a Pt/$TiO_2$ Catalyst on the Reverse Water Gas Shift Reaction," *Environmental Technology* 42, no. 2 (2021): 182–192.

30. G. Zhou, F. Xie, L. Deng, G. Zhang, and H. Xie, "Supported Mesoporous Cu/$CeO_{2-\delta}$ Catalyst for $CO_2$ Reverse Water–Gas Shift Reaction to Syngas," *International Journal of Hydrogen Energy* 45, no. 19 (2020): 11380–11393.

31. K. Lorber, I. Arčon, M. Huš, et al., "Light-Assisted Catalysis and the Dynamic Nature of Surface Species in the Reverse Water Gas Shift Reaction Over Cu/$\gamma$-$Al_2O_3$," *ACS Applied Materials & Interfaces* 16, no. 49 (2024): 67778–67790.

32. A.-A. Upadhye, I. Ro, X. Zeng, et al., "Plasmon-Enhanced Reverse Water Gas Shift Reaction Over Oxide Supported Au Catalysts," *Catalysis Science & Technology* 5, no. 5 (2015): 2590–2601.

33. K. Lorber, V. Shvalya, J. Zavašnik, et al., "Non-Oxidative Calcination Enhances the Methane Dry Reforming Performance of Ni/$CeO_{2-x}$ Catalysts Under Thermal and Photo-Thermal Conditions," *Journal of Materials Chemistry A* 12, no. 31 (2024): 19910–19923.

34. A. Marimuthu, J. Zhang, and S. Linic, "Tuning Selectivity in Propylene Epoxidation by Plasmon Mediated Photo-Switching of Cu Oxidation State," *Science* 339, no. 6127 (2013): 1590–1593.

35. C.-L. Ye, C.-L. Guo, and J.-L. Zhang, "Highly Active and Stable $CeO_2$-$SiO_2$ Supported Cu Catalysts for the Hydrogenation of Methyl Acetate to Ethanol," *Fuel Processing Technology* 143 (2016): 219–224.

36. B. Xie, R.-J. Wong, T.-H. Tan, et al., "Synergistic Ultraviolet and Visible Light Photo-Activation Enables Intensified Low-Temperature Methanol Synthesis Over Copper/Zinc Oxide/Alumina," *Nature Communications* 11, no. 1 (2020): 1615.

37. D. Fernández-Torre, J. Carrasco, M.-V. Ganduglia-Pirovano, and R. Pérez, "Hydrogen Activation, Diffusion, and Clustering on $CeO_2$(111): A DFT+ U Study," *Journal of Chemical Physics* 141, no. 1 (2014): 014703.

38. L. Álvarez-Falcón, F. Viñes, A. Notario-Estévez, and F. Illas, "On the Hydrogen Adsorption and Dissociation on Cu Surfaces and Nanorows," *Surface Science* 646 (2016): 221–229.

39. M. Kitano, S. Kanbara, Y. Inoue, et al., "Electride Support Boosts Nitrogen Dissociation Over Ruthenium Catalyst and Shifts the Bottleneck in Ammonia Synthesis," *Nature Communications* 6 (2015): 6731.

40. F. Jiang, S. Wang, B. Liu, et al., "Insights Into the Influence of $CeO_2$ Crystal Facet on $CO_2$ Hydrogenation to Methanol over Pd/$CeO_2$Catalysts," *ACS Catalysis* 10, no. 19 (2020): 11493–11509.

41. P. Djinović, J. Batista, and A. Pintar, "Calcination Temperature and CuO Loading Dependence on CuO–$CeO_2$ Catalyst Activity for Water-Gas Shift Reaction," *Applied Catalysis, A: General* 347, no. 1 (2008): 23–33.

42. Z. Yang, M. Zeng, K. Wang, et al., "Visible Light-Assisted Thermal Catalytic Reverse Water Gas Reaction Over Cu–$CeO_2$: The Synergistic of Hot Electrons and Oxygen Vacancies Induced by LSPR Effect," *Fuel* 315 (2022): 123186.

43. W.-H. Weber, K.-C. Hass, and J.-R. McBride, "Raman Study of $CeO_2$. Second-Order Scattering, Lattice Dynamics, and Particle-Size Effects," *Physical Review B* 48, no. 1 (1993): 178–185.

44. C. Schilling, A. Hofmann, C. Hess, and M.-V. Ganduglia-Pirovano, "Raman Spectra of Polycrystalline $CeO_2$: A Density Functional Theory Study," *Journal of Physical Chemistry C* 121, no. 38 (2017): 20834–20849.

45. P. Makuła, M. Pacia, and W. Macyk, "How To Correctly Determine the Band Gap Energy of Modified Semiconductor Photocatalysts Based on UV–Vis Spectra," *Journal of Physical Chemistry Letters* 9, no. 23 (2018): 6814–6817.

46. F. Zhang, Z. Liu, X. Chen, et al., "Effects of Zr Doping into Ceria for the Dry Reforming of Methane over Ni/$CeZrO_2$ Catalysts: In Situ Studies With XRD, XAFS, and AP-XPS," *ACS Catalysis* 10, no. 5 (2020): 3274–3284.

47. J. Liqiang, Q. Yichun, W. Baiqi, et al., "Review of Photoluminescence Performance of Nano-Sized Semiconductor Materials and Its Relationships With Photocatalytic Activity," *Solar Energy Materials and Solar Cells* 90, no. 12 (2006): 1773–1787.

48. G. Žerjav, M. Roškarič, J. Zavašnik, J. Kovač, and A. Pintar, "Effect of Au Loading on Schottky Barrier Height in $TiO_2$ + Au Plasmonic Photocatalysts," *Applied Surface Science* 579 (2022): 152196.

49. G.-N. Vayssilov, M. Mihaylov, P.-S. Petkov, K.-I. Hadjiivanov, and K.-M. Neyman, "Reassignment of the Vibrational Spectra of Carbonates, Formates, and Related Surface Species on Ceria: A Combined Density Functional and Infrared Spectroscopy Investigation," *Journal of Physical Chemistry C* 115, no. 47 (2011): 23435–23454.

50. N.-C. Nelson, M.-T. Nguyen, V.-A. Glezakou, R. Rousseau, and J. Szanyi, "Carboxyl Intermediate Formation via an In Situ-Generated Metastable Active Site During Water-Gas Shift Catalysis," *Nature Catalysis* 2 (2019): 916–924.

51. K. Mudiyanselage, A.-E. Baber, Z. Liu, S.-D. Senanayake, and D.-J. Stacchiola, "Isolation and Characterization of Formates on CeO–Cu O/Cu(1 1 1)," *Catalysis Today* 240, Part B (2015): 190–200.

52. C. Ledesma, J. Yang, D. Chen, and A. Holmen, "Recent Approaches in Mechanistic and Kinetic Studies of Catalytic Reactions Using SSITKA Technique," *ACS Catalysis* 4, no. 12 (2014): 4527–4547.

53. F. Meunier, D. Reid, A. Goguet, et al., "Quantitative Analysis of the Reactivity of Formate Species Seen by DRIFTS Over a Au/Ce(La)$O_2$ Water-Gas Shift Catalyst: First Unambiguous Evidence of the Minority Role of Formates as Reaction Intermediates," *Journal of Catalysis* 247, no. 2 (2007): 277–287.

54. L. Zhou, D.-F. Swearer, C. Zhang, et al., "Quantifying Hot Carrier and Thermal Contributions in Plasmonic Photocatalysis," *Science* 362, no. 6410 (2018): 69–72.

55. M.-B. Ansari and S.-E. Park, "Carbon Dioxide Utilization as a Soft Oxidant and Promoter in Catalysis," *Energy & Environmental Science* 5, no. 11 (2012): 9419.

56. Z. Zhao, M. Uddi, N. Tsvetkov, B. Yildiz, and A.-F. Ghoniem, "Enhanced Intermediate-Temperature $CO_2$ Splitting Using Non-stoichiometric Ceria and Ceria–Zirconia," *Physical Chemistry Chemical Physics* 19, no. 37 (2017): 25774–25785.

57. P.-G. Lustemberg, M.-V. Bosco, A. Bonivardi, H.-F. Busnengo, and M.-V. Ganduglia-Pirovano, "Insights Into the Nature of Formate Species in the Decomposition and Reaction of Methanol over Cerium Oxide Surfaces: A Combined Infrared Spectroscopy and Density Functional Theory Study," *Journal of Physical Chemistry C* 119, no. 37 (2015): 21452–21464.

## Supporting Information

Additional supporting information can be found online in the Supporting Information section.
Supporting Information.